In situ mechanical resonance behaviour of pristine and defective zinc blende GaAs nanowires

Edmund Pickering,[1] Arixin Bo,[1] Haifei Zhan,[2] Xiaozhou Liao,[3] Hark Hoe Tan[4] and YuanTong Gu[1*]

[1]*School of Chemistry, Physics and Mechanical Engineering, Queensland University of Technology (QUT), Brisbane, 4000, Australia*

[2]*School of Computing, Engineering and Mathematics, Western Sydney University, Locked Bag 1797, Penrith NSW 2751, Australia*

[3]*School of Aerospace, Mechanical and Mechatronic Engineering, The University of Sydney, NSW 2006, Australia*

[4]*Department of Electronic Materials Engineering, Research School of Physics and Engineering, The Australian National University, Canberra, ACT 2601, Australia*

**Author to whom correspondence should be addressed. Email:* yuantong.gu@qut.edu.au

† Electronic Supplementary Information (ESI) available: Expanded in situ resonance methodology. Scanning electron microscope videos showing (V1) an asymmetric resonant profile and (V2) a typical symmetric resonant profile. Comparison of damping effects and quality factor. Stiffness tensor comparison of zinc blende and wurtzite GaAs.

Abstract

The structural versatility of semiconducting gallium arsenide (GaAs) nanowires (NWs) provides an exciting avenue for engineering of their mechanical and dynamic properties. However, the dynamic behaviour of GaAs NWs remains unexplored. In this study, we conduct comprehensive *in situ* mechanical resonance tests to explore the dynamic behaviour of pristine and defective zinc blende GaAs NWs. The effects of stacking faults (SFs), amorphous shell, NW tapering and end-mass particles are investigated. The quality factors (QFs) of GaAs NWs are found to be predominately governed by surface effects, increasing linearly with the volume to surface-area ratio. Interestingly, SFs are found not influence QF. To extract the mechanical properties, Euler-Bernoulli beam theory is modified, incorporating the core-shell model, NW tapering and end-mass particles. It is found that the core-shell model accurately predicts the mechanical properties of the pristine GaAs NWs, which exhibit significant stiffening at radii below 50 nm. Conversely, the mechanical properties of the defective NWs are influenced by the presence of SFs, causing a wide variance in Young's modulus. Apart from establishing an understanding of the resonance behaviour of GaAs NWs, this work provides guidance in the design of NWs for their applications in dynamic nanomechanical devices with tailorable dynamic properties.

Keywords: GaAs, nanowire, mechanical resonance, stacking fault, quality factor, electrostatic probe

1. Introduction

The investigation of semiconducting materials at the nanoscale is of great significance in the continuous development of nanoscale devices such as nanoelectronic devices. Extensive research works have shown that nanomaterials exhibit properties that are greatly superior to in their bulk form.[1] Of this, type III-V semiconducting nanowires (NWs) are an important family of nanomaterials due to their desirable mechanical and electronic properties which can also be controlled and tailored to match targeted applications.[2] Within this, GaAs NWs are of growing interest due to their high mechanical flexibility,[3] controllable crystalline structure[4,5] and tuneable band gap,[6,7] endowing them with large potential in applications such as high-efficiency solar cells[8] and plasmonics.[9] To facilitate the successful implementation of NWs in various applications, a comprehensive understanding of their mechanical properties is usually a key prerequisite. As such, for the successful implementation of GaAs NWs, investigation of their mechanical behaviour under various loading conditions becomes a preliminary task.

To date, several works have reported the mechanical properties of GaAs NWs. A majority of these studies have focused on uniaxial compression and buckling tests,[3,10–12] where GaAs NWs have been shown to withstand ~11% strain.[3] Additionally, a strong size effect is observed in GaAs NWs due to the formation of an amorphous oxide shell, which induces an increase in effective Young's modulus at reduced diameters.[3,10] Such size effects become evident under buckling at diameters below 100 nm. GaAs NWs have also been reported to exhibit reversible plastic deformation governed by dislocation motion[13] and self-healing characteristics.[12]

Along with properties of static loading, the dynamic behaviour of NWs is also of significant importance. In this regard, the quality factor (QF) is commonly adopted to measure the damping effect during mechanical resonance. High QF NWs are a critical challenge in the development of high-frequency nanomechanical systems such as nanomechanical resonators.[14–18] As such, the investigation of existing and novel NW candidates, as well as the morphological and structural mechanisms which govern QF, is essential to the development of nanomechanical resonator devices. For instance, GaN NWs, another III-V semiconductor, have shown an apparent diameter dependence, with a QF of 500 – 2800 for diameter between 47 – 84 nm[19] and 2700 – 60 000 for diameter ranging from 100 to 500 nm.[16] However, no work has been conducted to assess the QF or dynamic behaviour of GaAs NWs, though they are showing broad appealing applications.

Of further interest is tailoring the crystalline structure of GaAs NWs, and understanding its effect on mechanical behaviour. GaAs commonly presents in two phases, zinc blende (ZB) or wurtzite (WZ),[20] however only the ZB is found in bulk, while both ZB and WZ structures can be selected for during synthesis. Additionally, through control of the growth rate, GaAs NW can be synthesised with a high density of stacking faults (SF),[21,22] which can be adopted to tune its mechanical properties.[10,23] As an example, Chen *et al.*[10] found that the presence of SF could increase the effective Young's modulus of WZ GaAs NW by ~13%. However, while the introduction of SFs has been demonstrated to be a

valuable route for tailoring of WZ GaAs mechanical properties, the effect of SFs on the mechanical properties of ZB GaAs NWs has not been investigated.

Clear gaps are present in the knowledge of GaAs NWs, specifically the dynamic behaviour of GaAs NWs, and the effect of SF on the mechanical behaviour of ZB GaAs NWs. To this end, we utilise an *in situ* mechanical resonance test to explore the resonance behaviour of ZB GaAs NWs with and without SFs. Through this, we extract the resonant spectrum of individual NWs, allowing for QF characterisation. Additionally, we developed a modified Euler-Bernoulli beam theory (EBT), through which we explored the influence of SFs, end-mass particles, and taper ratio on the resonance behaviour of ZB GaAs NWs. This study establishes a fundamental understanding of the resonance properties of GaAs NWs and the influence of SFs on their mechanical behaviour, which would shed light on their applications in future nanoscale devices.

2. Methodology

2.1. Synthesis and characterisation

To investigate the mechanical and dynamic properties of ZB GaAs NWs, pristine and defective samples were synthesised. The defective samples had a high density of SFs. This synthesis was conducted via Au-catalysed vapour-liquid-solid growth in a metalorganic chemical vapour deposition system. Details of the growth process can be found in reference [21]. For simplification, we henceforth use S-PR and S-SF to refer to NWs of the pristine and defective structures respectively. For synthesis, ZB GaAs NWs were epitaxially grown on a (111)B GaAs substrate using a two-step growth process.[21] First, a short-duration high-temperature nucleation process was conducted, followed by an extended low-temperature growth stage. This two-stage process promotes the successful formation of epitaxial GaAs NWs, while preventing SF formation. To synthesise ZB GaAs NWs with a high density of SF, the second stage growth temperature was raised. In addition to SF formation, this also promotes radial growth, and as such vertically-tapered NWs were formed. The crystalline structure of the specimens were characterised using a JEOL2100 transmission electron microscopy (TEM) operated at 200 kV.

2.2. *In situ* resonance

To investigate the dynamic behaviour of NWs, an *in situ* resonance technique was developed. Testing took place within a dual-beam scanning electron microscope (SEM), focused ion-beam system, and the electrostatic probe (ESP) actuation method was employed. For resonance, an ESP was brought into the proximity of a target NW, as is shown in Fig 1. Through the application of an AC voltage to the ESP, a cyclic force developed between the ESP and target NW. This approach allowed for fine control of the force's frequency, necessary for the analysis of dynamic properties. Further detail on this methodology is provided in the ESI†.

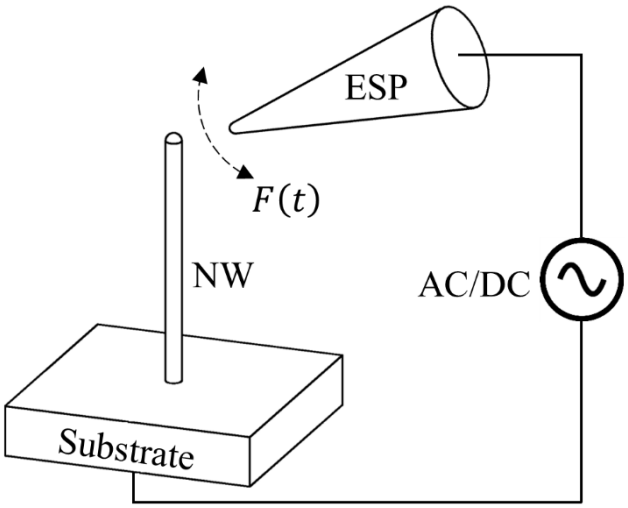

Fig 1. Schematic illustration of resonance protocol showing the cyclic force, *F(t)*, between the ESP and NW as a result of an AC/DC voltage.

During testing, the NWs were observed via SEM. Resonant frequencies were manually located, with care being taken to identify the correct mode and avoid erroneous results from parametric resonance[24] (see ESI†). In tests where the resonant spectrum was desired, a frequency sweep was performed and a video micrograph was recorded. The frequency-amplitude spectrum was then extracted through an in-house image processing code. A full resonant spectrum was measured only for a limited number of representative samples due to experimental complexity.

3. Results and discussion

3.1. Structural and morphological characterisation

The samples were characterised via SEM and TEM techniques to confirm the morphology, crystallographic structure and defects, this is shown in Fig 2. In Fig 2(a) and (b), it is shown that both samples were successfully grown epitaxial NWs. As seen, S-PR NWs exhibits large slenderness, with lengths ranging from 14 – 16 µm and diameters between 200 – 400 nm with minimal tapering; a typical S-PR NW is presented in Fig 2(c). Alternatively, S-SF NWs exhibit a clear tapered morphology as shown in Fig 2(d); specifically, the length, mean diameter, and taper angle of S-SF NWs range between 5 – 16 µm, 60 – 260 nm, and < 1.5°, respectively. There is a strong correlation between taper angle and SFs in GaAs NWs, signifying the presence of SFs in the tapered NWs.[10,21] S-SF NWs additionally presents an enlarged pyramidal fixture as a result of the two-stage growth process. The pyramid-shaped base was considered part of the substrate and was excluded from the dimension measurement of the NWs. The cross-section of both S-PR and S-SF NWs is circular. Both samples contain an Au particle at their tip.

To conduct crystalline structure analysis, NWs were mechanically transferred to Cu TEM grids. Through TEM imaging, S-SF NWs were verified to have a high density of SFs, as illustrated in Fig 2(f) where the SFs are clearly indicated by lines of dark contrast orthogonal to the growth direction.[10,22] In comparison, no such SFs were found in the S-PR NWs, as shown in Fig 2(e). For both samples, a gold particle is clearly seen as a dark semicircle at the top of each NW, shown in Fig 2(e) and (f). Furthermore, high-resolution TEM (HRTEM) micrographs show that S-PR NWs have a uniform, single-crystalline structure free from defects as shown in Fig 2(g). Conversely, S-SF NWs clearly show SFs, as marked by the black dashed line in Fig 2(h). To confirm the crystalline structure, we present selected area electron diffraction (SAED) patterns of both samples in theinsets of Fig 2(g) and (h). These SAED fit well with the patterns expected from the $[10\bar{1}]$ zone axis of ZB GaAs.[20,25] In the case of S-SF NWs, the SAED patterns shows notable streaking in the growth direction, this streaking is indicative of SFs in the NWs.[10,26] The SAED in combination with the HRTEM shows both samples are grown along the [111] direction. Finally, both S-PR and S-SF NWs have a uniform amorphous oxide layer which forms upon exposure to atmosphere. According to the HRTEM micrograph, the oxide layer is measured to be approximately 2 nm. The crystalline structure of ZB GaAs is presented in Fig 2(i).

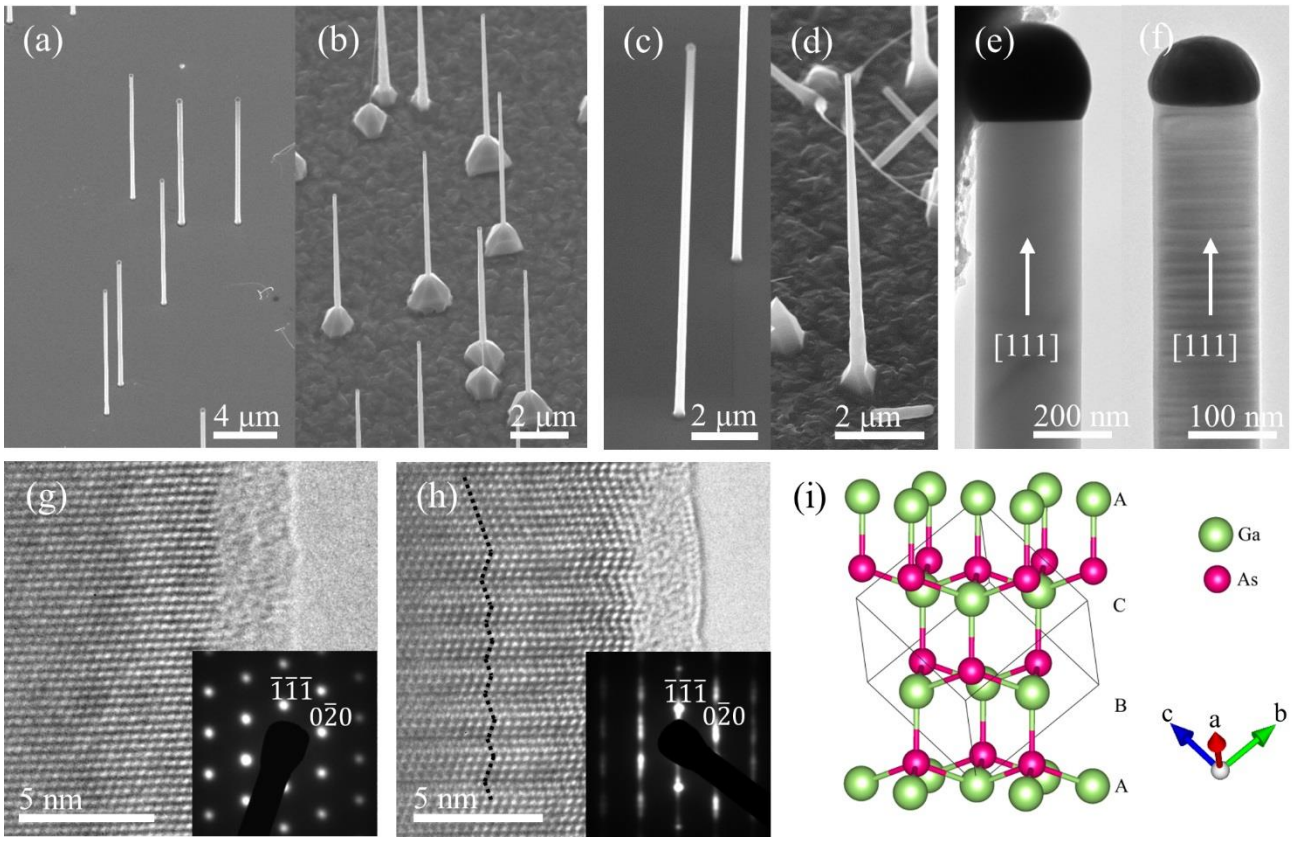

Fig 2. Morphological and crystalline structure of S-PR and S-SF GaAs NWs respectively; (a, b) low magnification SEM micrograph of S-PR and S-SF NWs; (c, d) high resolution SEM micrograph of S-PR and S-SF NWs; (e, f) TEM micrograph of S-PR and S-SF NWs; (g, h) HRTEM micrographs of S-PR and S-SF NWs, the dotted line in (h) shows stacking faults; insets show SAED along the $[10\bar{1}]$ zone

axis; (i) crystalline structure of ZB GaAs built using VESTA,[27] with the stacking order indicated (structure obtained from reference [25]).

3.2. Mechanical resonance

Mechanical resonance was readily obtained for both S-PR and S-SF NWs, with S-PR NWs exhibiting a mean 1st mode resonant frequency of 744 kHz with a standard deviation (σ) of 208 kHz across a sample number (n) of 39. In comparison, S-SF NWs exhibited a mean 1st mode resonant frequency of 3833 kHz (σ = 1435 kHz, n = 38); the significantly larger resonant frequency of S-SF can be predominantly attributed to their shorter length and smaller diameters as detailed in the structural characterisation section. All tested NWs showed resonance, with the majority of the results being collected at a driving voltage of 0.5 – 1 V_{pp}, while low-amplitude resonance was still identifiable at driving voltages of 0.02 V_{pp}. Fig 3(a) presents an SEM micrograph of a resonating NW under the driving force of the ESP with the static state shown in the inset. Likewise, Fig 3(b) presents a typical resonance spectrum of a GaAs NW, showing the expected behaviour of a mechanical resonator.

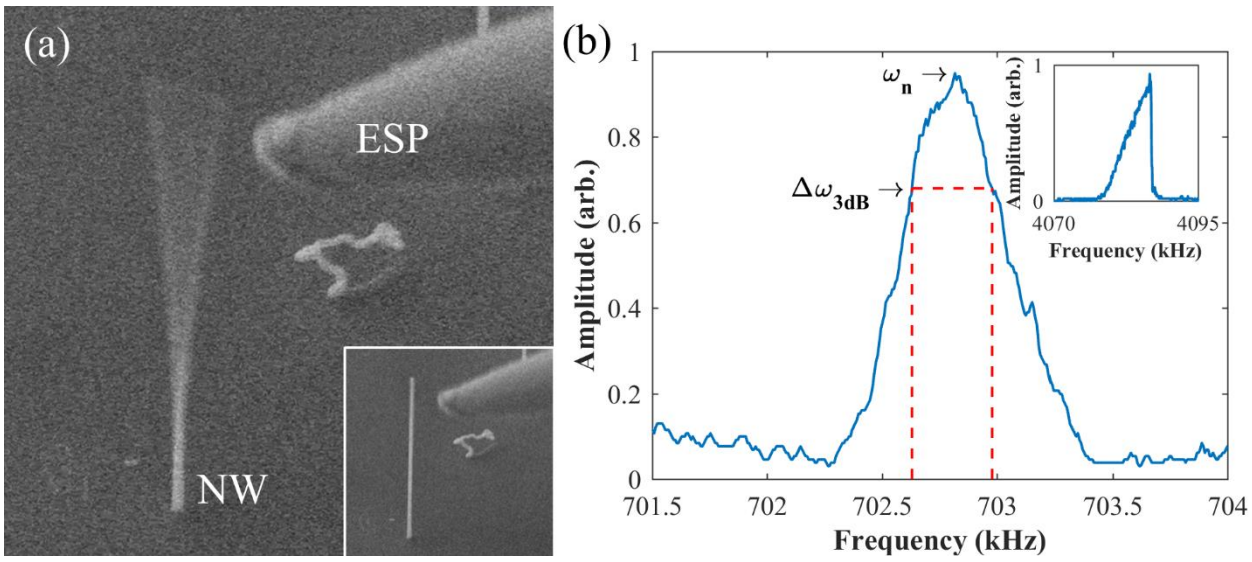

Fig 3. (a) An SEM micrograph showing resonance of a S-PR NW (inset shows the static state), and (b) a typical frequency-amplitude spectrum for a GaAs NW showing the natural frequency (ω_n) and half-power bandwidth ($\Delta\omega_{3dB}$); inset shows a frequency-amplitude spectrum exhibiting hysteresis.

During large amplitude NW resonance, a hysteresis effect was commonly detected which manifests as an asymmetric resonance curve in which following the point of maximum amplitude the vibration amplitude suddenly drops to zero; this is shown in the Fig 3(b) inset and a video is provided in the ESI† V1. Both S-PR and S-SF presented this behaviour at large driving voltages and deflections. Likewise, this asymmetric effect was observed to disappear when the voltage and deflection amplitude was reduced (ESI† V2). This phenomenon can be attributed to non-linearity in the mechanical behaviour at high driving-voltages and deflections resulting in unstable segments of the resonance

spectrum.[28–30] Therefore, care should be taken during data acquisition to avoid this hysteresis effect by ensuring low driving voltages and deflections.

3.3. Quality factor

As discussed, a key advantage of the resonance test is that it allows for the direct measurement of QF which is indicative of the internal damping of a material. Depending on the methodology being applied, there are several definitions of QF. In this work, the QF is defined as the natural frequency (ω_n) over the half-power bandwidth ($\Delta\omega_{3dB}$); i.e. $Q = \omega_n/\Delta\omega_{3dB}$. Fig 4 compares the QF of the examined S-PR and S-SF NWs. As is seen, S-PR NWs exhibit a QF in the range of 1292 – 3156, while the S-SF NWs shows a much lower QF in the range of 442 – 1371. A large variance in QF is observed for both samples, though this is expected and is in line with other similar works.[15,16,19,28] For the diameter range tested, an apparent size dependence was observed between the QF and NW radius, with QF appearing to increasing linearly with radius. Interestingly, this relationship appears similar for both S-PR and S-SF NWs, suggesting that for ZB GaAs NWs, QF is largely independent of SFs and is rather a factor of geometry.

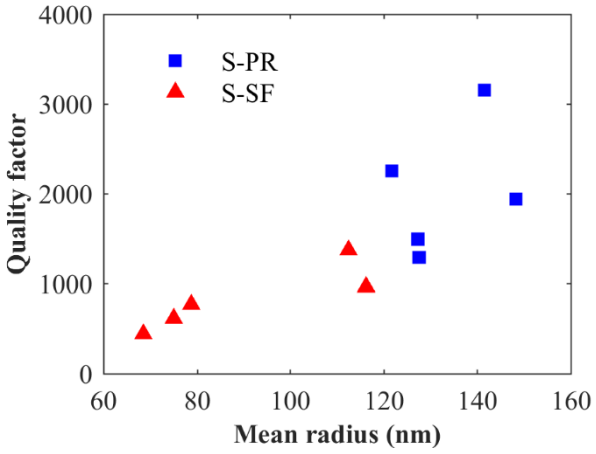

Fig 4. QF of S-PR and S-SF NWs as measured through the resonance test, showing an apparent size dependence of QF.

To appropriately investigate the mechanism of this size dependence, the various contributors to QF were analysed. In general, the overall QF is composed of both intrinsic and extrinsic damping factors, with the main factors being thermo-elastic damping, gas damping, fixture effects, and surface effects,[14] these inversely summate to give the overall QF as $Q_{total}^{-1} = Q_{thermo-elastic}^{-1} + Q_{gas}^{-1} + Q_{fixture}^{-1} + Q_{surface}^{-1} + \cdots$ [31].

Thermo-elastic damping is caused by internal friction within a material and a coupling between the mechanical stress field and the temperature field. According to Zener's[32] model, thermo-elastic damping is negligible when the characteristic time of thermal diffusion through the NW diameter is much greater than the resonant period ($\alpha/d^2 \gg \omega_1^{-1}$, where α is the thermal diffusivity and d is the

NW diameter).[15] This criteria is met in this work, and as such thermo-elastic damping can be neglected. Furthermore, as any influence of SFs on QF would manifest through thermos-elastic damping, it can be concluded that SFs have little effect on QF. This work was conducted at pressures below 5 mPa, here gas damping is governed by the molecular regime where the gas damping is a result of momentum transfers from individual collisions of gas molecules with the resonator.[14] At this range, the QF contribution of gas damping is negligible, this is supported by Bartolomé et al.[14] Energy losses as a result of the fixture manifest from elastic waves propagating through the fixture, i.e. the damping effect is dependent on fixture geometry and NW aspect ratio. However, Photiadis and Judge[33] show that for the dimensions in this work, the overall effect of fixture damping is negligible. Thus, as it can be shown that other forms of damping are negligible, it can be concluded that the key contributor to QF for our resonance test is the surface effects. This is in line with other literature which has found that for NW resonators, QF is dominated by surface effects.[16,34] Further detail and justification of this, including theoretical modelling, is provided in the ESI†.

In the case of surface effects, energy is stored in the NW as strain energy and dissipated at the surface,[29] making the QF dependent on the ratio of volume to surface-area ($k_{vs} = V/S$).[35] For a non-tapered NW, with a circular cross-section, the volume to surface-area ratio is $r/2$, where r is the mean radius. For a tapered NW, the volume to surface-area ratio is dependent on the taper ratio ($t = a/b$) where a and b are the radii of the free and fixed ends, respectively. When the NW length is much larger than the mean radius ($L \gg r$), the k_{vs} of a tapered NW can be simplified to $r/2 \times (4/3)(t^2 + t + 1)/(t^2 + 2t + 1)$. However, across the taper rations present in this study (t = 0.35 – 1.0), k_{vs} changes by less than 8%, meaning NW radius is more significant than taper ratio. Thus, the NW radius is the main variable governing k_{vs}. Through this, our results show that in meeting the challenge of high QF nanoresonators, a focus should be placed on surface effects, as governed by the volume to surface-area ratio.

3.4. Young's modulus

To further explore the mechanical properties of GaAs NWs, we investigated the effect of SFs on Young's modulus. Theoretically, the resonance behaviour of a NW can be described by beam models. Previous studies have shown that EBT provides a good description of resonating NWs.[17,19] However, standard EBT does not account for the combined effects of an amorphous shell, end-mass particles or tapering, all of which are significant. For this reason, we perform several modifications. First, we consider the case of S-PR NWs, which do not exhibit tapering. For these the core-shell model is adopted to describe the amorphous oxide layer, this applies different Young's moduli to the core and shell of the NW.[24] To account for the Au particle end-mass Dunkurley's method[36] is applied, approximating the Au particle to be a spherical particle with radius equal to the NW free-end radius. Combining these, the first natural frequency ($\omega_{1,SP}$) of a uniform NW can be expressed as:[36]

$$\omega_{1,SP} \cong \sqrt{\frac{3(EI)^*}{(0.243\rho AL + m_p)L^3}} \quad (1)$$

where SP refers to the modifications for the amorphous surface layer and end-mass particle, ρ is the NW density, A is the cross-sectional area, L is the length, m_p is the end particle mass and $(EI)^*$ is the effective bending rigidity of the NW.[36] The effective bending rigidity is the summation of core and shell rigidities, i.e., $(EI)^* = E_c I_c + E_s I_s$, where E and I are the Young's modulus and second moment of area of the core and shell respectively. The density of ZB GaAs is 5317 kg/m^3 (PDF 00-014-0450[37]).

Analysis of the S-SF NWs is more complex as currently EBT has not yet been extended to cover the resonance of tapered core-shell beams. Thus, as an approximate solution, we develop a model based upon the analytical solution of a linearly-tapered beam, employing Dunkerley's method to account for the end-mass particle. For such a beam, without an end-mass particle, Conway and Dubil[38] and Blevins[39] have derived the first natural frequency to be $\omega_1 \cong \beta_t^2\sqrt{(EI_0)/(\rho A_0 L^4)}$ (for a circular cross-section fixed at its larger end). Here, I_0 and A_0 refer to the second moment of area and the area of the fixed end respectively. β_t^2 is the Eigen-solution corresponding to the first mode which can be approximated by $\beta_t^2 \cong 8.72\sqrt{(1-0.016t)/(1+5.053t)}$.

Dunkerley's method[36] states the approximate fundamental frequency of a multi-degree-of-freedom system to be $\omega_1 = (\omega_{11}^{-2} + \omega_{22}^{-2} + \cdots)^{-1/2}$, where ω_{11}, ω_{22}, etc., are the natural frequencies of the systems when each mass is considered to be acting in the absence of other inertial terms. For small deflection, the rigidity of a tapered cantilever is $3EI_0/(L^3 t)$. Thus, neglecting the inertia of the beam, the natural frequency of a tapered cantilever with an end-mass is $\sqrt{3EI_0/(L^3 m_p t)}$. As such, applying Dunkerley's method, the first natural frequency of a tapered, core-shell, cantilevered beam with an end mass can be estimated as:

$$\omega_{1,TP} \cong \beta_t^2\sqrt{\frac{3E^*I_0}{L^3(3\rho A_0 L + \beta_t^4 m_p t)}} \quad (2)$$

where TP refers to the modifications for the tapering and end-mass particle and other variables are as already defined. Hereafter we refer to this modified EBT, incorporating the surface layer and the end-mass particle, as EBT-TP.

EBT-TP provides a notable improvement when considering the effects of tapering and end-mass particles. To illustrate this, in Fig 5, we examine the effects of tapering and end-mass particles on the predicted first-mode resonant frequency. For this, consider a representative ZB GaAs NW with an effective Young's modulus equivalent to bulk ZB GaAs (140 GPa[40]), a length of 12 μm, and a gold end-mass particle equal to the tip radius. For this analysis, taper ratios of 1.0 (no taper), 0.7, and 0.4 are used, in line with the NWs present in this work. As compared in Fig 5, tapering has a significant impact

on the predicted resonant frequency. For instance, at a mean radius of 200 nm, the resonant frequency of the NW without tapering is more than two times higher than its counterpart with a taper ratio of 0.4. Critically, this is equivalent to a tapering of 0.5° along the NW length, which signifies the important influence tapering can have on the resonant frequencies of NWs. Moreover, the tapering effect appears more significant for NWs with larger mean radius. In comparison, for all three taper ratios, the end-mass particle acts to reduce the resonant frequency, however is less significant than taper ratio. Additionally, the influence of the end-mass particle increases with increasing mean radius, due to the larger particle mass.

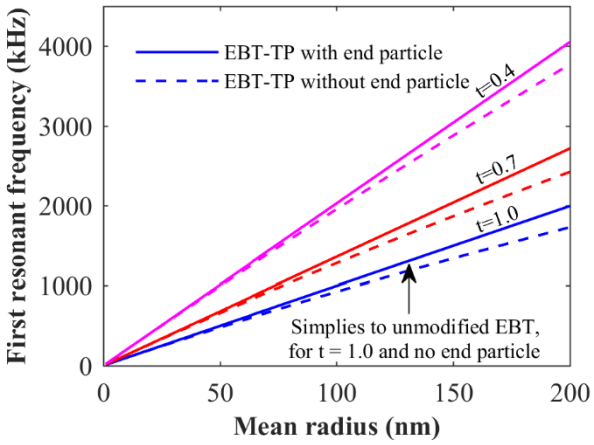

Fig 5. Prediction of EBT-TP, comparing the influence of taper ratio and end-mass particle on the first resonant frequency of NWs. Solid and dashed lines respectively represent the theoretical model including or neglecting the influence of the end-mass particle. For a taper ratio of t = 1.0 and no end-mass particle, EBT-TP simplifies to the unmodified EBT.

Based on our modified EBT model, equations (1) and (2), the effective Young's modulus of the S-PR and S-SF NWs are derived and compared in Fig 6. In detail, S-PR NWs show a strong size dependent Young's modulus, which approaches the bulk value when the NW mean radius is above 100 nm. The core and shell Young's modulus can be determined by fitting the core-shell model, $(EI)^* = E_c I_c + E_s I_s$, to the effective Young's modulus as demonstrated in Fig 6. Through this, utilising the measured shell thickness of 2 nm, the core and shell Young's modulus are determined to be 154 and 555 GPa respectively. Our measured core Young's modulus is also close to that of the bulk form in the same crystallographic direction (149 GPa[40], see ESI†). For S-SF NWs, a wide variance of effective Young's modulus is observed. As shown by Chen *et al.*,[10] SFs can affect the Young's modulus of NWs. We propose that the variance in effective Young's modulus of S-SF NWs is due to different SF densities in the examined samples. It is further proposed that this variance in effective Young's modulus has masked any clear size-dependent effects which would be expected due to the amorphous shell. Unfortunately, *in situ* SEM testing does not allow for the quantification of SF density for tested samples, further efforts are expected to address this.

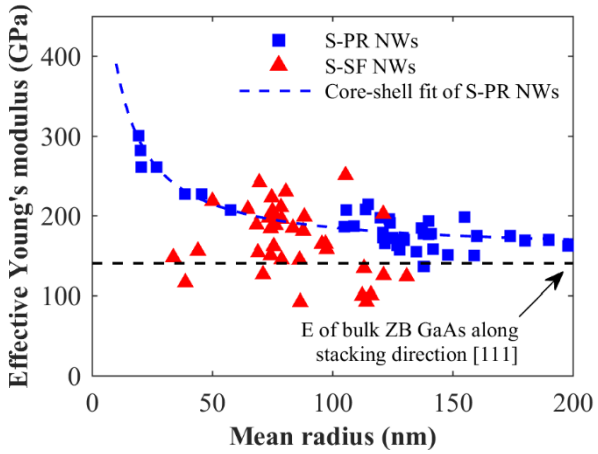

Fig 6. Young's modulus of S-PR and S-SF NWs as measured through the resonance test.

It is worth noting that the theoretical stiffness tensor[40] predicts that both pristine ZB and WZ GaAs NWs have the same Young's modulus in the stacking direction (see ESI †). To investigate this further, we compare our calculated core and shell Young's modulus of ZB GaAs NWs (154 and 555 GPa respectively) to that of WZ GaAs NWs (145 and 489 GPa respectively[10]). These results differ by 6% and 12%, respectively, confirming that both pristine ZB and WZ GaAs NWs display similar Young's modulus in the stacking direction. This is critical, as it suggests that from a Young's modulus perspective ZB and WZ GaAs NWs are equivalent, and thus to tailor the Young's modulus, a focus should be paid to the effect of defects such as SFs. However, further study is required to elucidate the mechanism by which SFs affect mechanical properties of GaAs as this is presently unclear.

4. Conclusions

In summary, we investigate, for the first time, the resonant behaviour of ZB GaAs NWs, with a focus on SF, tapering, and end-mass particles. This study shows that the QF of ZB GaAs NWs is governed by surface effects, increasing linearly with NW radius. As such, efforts to develop high QF nanoresonators should place a focus on damping due to surface effects. In addition, a modified EBT is developed allowing for the mechanical characterisation of tapered NWs with end-masses. Pristine ZB GaAs NWs are shown to have a strong size effect below radii of 100 nm, resulting is stiffening. Additionally, the Young's modulus of the core and amorphous shell were determined. Interestingly, the effective Young's modulus of pristine ZB GaAs NWs is found to be very similar to that of WZ GaAs NWs. Finally, SFs are shown to influence the Young's modulus of ZB GaAs NWs, suggesting they could become a valuable means of Young's modulus tailoring. However, more work is required to elucidate these mechanisms. These results provide exciting avenues for the engineering of GaAs NW mechanical and dynamic properties, which will aid in the implementation of GaAs NWs in nanomechanical devices such as nanomechanical resonators.

Conflicts of interest

There are no conflicts to declare.

Acknowledgements

The authors gratefully acknowledge and thanks the facilities and technical support of the Central Analytical Research Facility (CARF) at the Queensland University of Technology (QUT). We thank Australian National Fabrication Facility, ACT node for access to the growth facilities used in this work. We likewise thank Prof Chennupati Jagadish, Dr Qiang Gao, and Dr Yujie Chen for their synthesis and support. Finally, support from the ARC Discovery Project (DP170102861) are gratefully acknowledged.

Reference

1 Wang S, Shan Z, Huang H. The Mechanical Properties of Nanowires. Adv Sci. 2017;4(4):1–24.

2 Joyce HJ, Gao Q, Hoe Tan H, Jagadish C, Kim Y, Zou J, et al. III-V semiconductor nanowires for optoelectronic device applications. Prog Quantum Electron. 2011;35(2–3):23–75.

3 Wang YB, Wang LF, Joyce HJ, Gao Q, Liao XZ, Mai YW, et al. Super deformability and young's modulus of gaas nanowires. Adv Mater. 2011;23(11):1356–60.

4 Ihn SG, Song JI, Kim TW, Leem DS, Lee T, Lee SG, et al. Morphology- and orientation-controlled gallium arsenide nanowires on silicon substrates. Nano Lett. 2007;7(1):39–44.

5 Krogstrup P, Popovitz-Biro R, Johnson E, Madsen MH, Nygård J, Shtrikman H. Structural phase control in self-catalyzed growth of GaAs nanowires on silicon (111). Nano Lett. 2010;10(11):4475–82.

6 Heiss M, Conesa-Boj S, Ren J, Tseng HH, Gali A, Rudolph A, et al. Direct correlation of crystal structure and optical properties in wurtzite/zinc-blende GaAs nanowire heterostructures. Phys Rev B. 2011;83(4):1–10.

7 Ketterer B, Heiss M, Uccelli E, Arbiol J, Morral AFI. Untangling the Electronic Band Structure of Wurtzite GaAs Nanowires by Resonant Raman Spectroscopy. ACS Nano. 2011;5(9):7585–92.

8 Aberg I, Vescovi G, Asoli D, Naseem U, Gilboy JP, Sundvall C, et al. A GaAs nanowire array solar cell with 15.3% efficiency at 1 sun. IEEE J Photovoltaics. 2016;6(1):185–90.

9 Ho J, Tatebayashi J, Sergent S, Fong CF, Iwamoto S, Arakawa Y. Low-threshold near-infrared GaAs-AlGaAs core-shell nanowire plasmon laser. ACS Photonics. 2015;2(1):165–71.

10 Chen Y, Burgess T, An X, Mai Y-W, Tan HH, Zou J, et al. Effect of a High Density of Stacking Faults on the Young's Modulus of GaAs Nanowires. Nano Lett. 2016;16(3):1911–6.

11 Chen Y, Gao Q, Wang Y, An X, Liao X, Mai YW, et al. Determination of Youngs Modulus of Ultrathin Nanomaterials. Nano Lett. 2015;15(8):5279–83.

12 Wang Y, Joyce HJ, Gao Q, Liao X, Tan HH, Zou J, et al. Self-healing of fractured GaAs nanowires. Nano Lett. 2011;11(4):1546–9.

13 Bao P, Wang Y, Cui X, Gao Q, Yen HW, Liu H, et al. Atomic-scale observation of parallel development of super elasticity and reversible plasticity in GaAs nanowires. Appl Phys Lett. 2014;104(2).

14 Bartolomé J, Cremades A, Piqueras J. High quality factor indium oxide mechanical microresonators. Appl Phys Lett. 2015;107(19):191910.

15 Smith D a., Holmberg VC, Lee DC, Korgel B a. Young's modulus and size-dependent mechanical quality factor of nanoelectromechanical germanium nanowire resonators. J Phys Chem C. 2008;112:10725–9.

16 Tanner SM, Gray JM, Rogers CT, Bertness KA, Sanford NA. High-Q GaN nanowire resonators and oscillators. Appl Phys Lett. 2007;91(20):203117.

17 Shi Y, Chen CQ, Zhang YS, Zhu J, Yan YJ. Determination of the natural frequency of a cantilevered ZnO nanowire resonantly excited by a sinusoidal electric field. Nanotechnology. 2007;18(7):75709.

18 Bai XD, Gao PX, Wang ZL, Wang EG. Dual-mode mechanical resonance of individual ZnO nanobelts. Appl Phys Lett. 2003;82(26):4806–8.

19 Nam C-Y, Jaroenapibal P, Tham D, Luzzi DE, Evoy S, Fischer JE. Diameter-dependent electromechanical properties of GaN nanowires. Nano Lett. 2006;6(2):153–8.

20 McMahon MI, Nelmes RJ. Observation of a wurtzite form of gallium arsenide. Phys Rev Lett. 2005;95(21):18–21.

21 Joyce HJ, Gao Q, Tan HH, Jagadish C, Kim Y, Zhang X, et al. Twin-free uniform epitaxial GaAs nanowires grown by a two-temperature process. Nano Lett. 2007;7(4):921–6.

22 Shtrikman H, Popovitz-Biro R, Kretinin A, Houben L, Heiblum M, Bukala M, et al. Method for suppression of stacking faults in wurtzite III-V nanowires. Nano Lett. 2009;9(4):1506–10.

23 Chen B, Wang J, Gao Q, Chen Y, Liao X, Lu C, et al. Strengthening brittle semiconductor nanowires through stacking faults: Insights from in situ mechanical testing. Nano Lett. 2013;13(9):4369–73.

24 Chen CQ, Shi Y, Zhang YS, Zhu J, Yan YJ. Size dependence of Young's modulus in ZnO nanowires. Phys Rev Lett. 2006;96(7):1–4.

25 Jain A, Ong SP, Hautier G, Chen W, Richards WD, Dacek S, et al. Commentary: The materials project: A materials genome approach to accelerating materials innovation. APL Mater. 2013;1(1).

26 Pozuelo M, Prikhodko S V., Grantab R, Zhou H, Gao L, Sitzman SD, et al. Zincblende to wurtzite transition during the self-catalyzed growth of InP nanostructures. J Cryst Growth. 2010;312(16–17):2305–9.

27 Momma K, Izumi F. VESTA 3 for three-dimensional visualization of crystal, volumetric and morphology data. J Appl Crystallogr. 2011;44(6):1272–6.

28 Ding W, Calabri L, Chen X, Kohlhaas KM, Ruoff RS. Mechanics of crystalline boron nanowires. Compos Sci Technol. 2006;66(9):1109–21.

29 Kacem N. Nonlinear Dynamics and Its Applications in Nanocantilevers. In:

Nanocantilever Beams: Modeling, Fabrication, and Applications. New York: Pan Stanford; 2016.

30 Shao LC, Palaniapan M, Tan WW. The nonlinearity cancellation phenomenon in micromechanical resonators. J Micromechanics Microengineering. 2008;18:65014.

31 Biedermann LB, Tung RC, Raman A, Reifenberger RG. Flexural vibration spectra of carbon nanotubes measured using laser Doppler vibrometry. Nanotechnology. 2009;20(3):35702.

32 Zener C. Internal Friction in Solids II. General Theory of Thermoelastic Internal Friction. Phys Rev. 1938 Jan;53(1):90–9.

33 Photiadis DM, Judge JA. Attachment losses of high Q oscillators. Appl Phys Lett. 2004;85(3):482–4.

34 Yang J, Ono T, Esashi M. Energy dissipation in submicrometer thick single-crystal silicon cantilevers. J Microelectromechanical Syst. 2002;11(6):775–83.

35 Jensen K, Girit C, Mickelson W, Zettl A. Tunable nanoresonators constructed from telescoping nanotubes. Phys Rev Lett. 2006;96(21):1–4.

36 Stephen NG. Vibration of a cantilevered beam carrying a tip heavy body by Dunkerley's method. J Sound Vib. 1980;70(3):463–5.

37 International Center for Diffraction Data (ICDD). PDF-4+ 2016 (Database). Kabekkodu S, editor. Newtown Square, PA, USA; 2016.

38 Conway HD, Dubil JF. Vibration Frequencies of Truncated-Cone and Wedge Beams. J Appl Mech. 1965 Dec 1;32(4):932–4.

39 Blevins RD. Natural Frequency of Beams. In: Formulas for Dynamics, Acoustics and Vibration. John Wiley & Sons, Ltd; 2015. p. 134–202.

40 Wang SQ, Ye HQ. First-principles study on elastic properties and phase stability of III - V compounds. Phys Status Solidi Basic Res. 2003;240(1):45–54.